Dynamic vibration absorber for the mitigation of potential wheel polygonization at trams

Journal of
Mechanical Engineering Science

DOI: ToBeAssigned
www.sagepub.com/
SAGE

Florian Zehetbauer[1], Johannes Edelmann[1], Alois Steindl[1], and Manfred Plöchl[1]

Abstract

Polygonal wheels are a widespread problem in the railway industry. Oscillation phenomena appearing at the wheelset may provide an environment where the wheel polygonization is promoted essentially. The flexibility of the wheelset was highlighted as an important influence on these phenomena in curves with a small radius of curvature at trams in recent studies. A dynamic vibration absorber applied on the wheelset may reduce oscillations at the wheelset significantly and is studied as a potential mitigation measure of wheel polygonization. A basic system model, representing a wheelset with non-driven independently rotating wheels, is used to investigate the mechanism and performance of this passive remedy. Influences of different parameter combinations of the absorber are discussed systematically. The efficiency of the dynamic vibration absorber is analysed further with a more detailed multibody system model of a two-axle tram bogie. Results reveal that an adequately tuned absorber might significantly reduce the possible development and further evolution of predominant polygonal orders. Additionally, basic guidelines for the design of the dynamic vibration absorber applied at the wheelset are pointed out.

Keywords

Railway wheel polygonization, Wheelset flexibility, Dynamic vibration absorber

Introduction

Polygonal wheels, which have a periodic irregularity around the wheel circumference superimposed on a constant wheel radius, are a type of wheel out-of-roundness (OOR). The phenomenon is found in a broad range of rolling stock vehicles, including high-speed vehicles, locomotives, freight wagons, metros, and trams. It is a fundamental problem in the railway industry, as out-of-round wheels excite the wheelset, especially in the vertical direction, resulting in a detrimental influence, e.g. ride comfort, vehicle and track components, life cycles of the wheels.

The literature points out that there are multiple generation mechanisms The state-of-the-art until 2003 is summarized in [1]. The review gives a classification of different types of defects on railway wheel tread and discusses reasons for the development of OOR railway wheels. Tao et al. presented potential causes, consequences, simulation methods, and potential mitigation measures to prevent wheel polygonization in a recent review paper [2]. This survey focuses on wheel polygonization in metro vehicles, locomotives, and high-speed trains in China. Characteristics, consequences, potential remedies, and development mechanisms of wheel polygonization at Chinese high-speed railway systems are discussed in [3]. A recent paper by Iwnicki et al., [4], reviews potential formation mechanisms, measurement methods, computer simulation techniques and potential mitigation methods.

The majority of researchers have the consensus that wheel polygonization is a consequence of a 'fixed-frequency' or a 'fixed wavelength' mechanism, and the underlying cause must be related to a resonance of the vehicle–track dynamic system. Influencing factors such as material hardness [5], initial imbalances of the wheelset [6], wheel flats [7], wheelset flexibility [2; 8–11], rail flexibility [12; 13], self-excitation [14–16], and P2 resonance [2; 13; 17] have been pointed out. The literature suggests that there might be different explanations for different types of rolling stock.

Trams differ from conventional railways essentially. Whereas conventional railway vehicles use almost exclusively solid-axle wheelsets, independently rotating wheels (IRW) are frequently found at trams. The use of wheelsets in the axlebridge design with independently rotating wheels, as shown in Figure 8 later, may allow consistently flat floors in the car body of low-floor trams. Resilient wheels may be applied to tram wheelsets for their beneficial effect on preventing squealing and impact noise [18]. In addition to the vehicles, the infrastructure of tramway networks features specific characteristics. A typical operation route contains a great variety of curves with small radius of curvature due to the urban structure and proximity of surrounding facilities. Phenomena emerging in curves with a small radius of curvature at tramways are addressed in this study, as high lateral creepages and thus intensive wear can arise in these curves.

A (not published) internal technical measurement report, [19], indicated that vibrations of wheelsets might occur during negotiating curves with a small radius of curvature at specific tram lines. Recurring periods of respective periodic wheelset oscillations of about ~ 50 Hz at typical speeds of 15–19 km/h are suggested to promote the measured wheel polygonization at tram wheels featuring 17 to 20 waves. A preliminary study, [20], indicated the possible appearance of self-excited vibrations at trams when negotiating a curve with a small radius of curvature. Key parameters

[1] Institute of Mechanics and Mechatronics, TU Wien, Austria

Corresponding author:
Florian Zehetbauer, TU Wien, Austria.
Email: florian.zehetbauer@tuwien.ac.at

that influence the onset of such self-excited vibrations and subsequent vibrational behaviour were identified by introducing an appropriate minimal model in a more detailed study, [16]. Results revealed that the negative slope in the creep force–lateral creepage characteristics is necessary but not sufficient for potential self-excitation for a realistic range of parameters. The combination and interaction of the motions between the resilient wheel and the wheelset axle are pointed out to be essential for the potential loss of stability and sustained self-excited vibrations. It is highlighted that the frequency of the unstable mode is related to the second bending mode of the wheelset. Necessary conditions to operate in the negative regime in the creep force–lateral creepage characteristics relate to the relationship between the angle of attack, the curve radius and the vehicle speed. Results also indicated that reducing the slope of the falling regime in the creep force–lateral creepage characteristics is likely to avoid unstable conditions and suppress subsequent self-excitation.

However, other potential excitation mechanisms, such as P2 resonance or forced excitations due to initial wheel OOR, might also excite the bending modes of the elastic wheelset axle, [2]. Wheel polygonization might develop from an initial, small amplitude wheel OOR, present on the running surface of railway wheels, even when they are new, to larger radius deviations with a dominant order due to wear in the wheel–rail interface [21]. In [10], the impact of tram characteristics on wheel polygonal wear evolution resulting from forced excitation due to initial wheel OOR is discussed. There, analysis of evolution tendency curves (ETC), which will also be addressed in this study, revealed that structural modes of the wheelset's axle, particularly the first and second bending mode, and the flexibility of the resilient wheel dominate the evolution of potentially predominant OOR orders in the frequency range of interest.

In order to suppress and/or reduce wheel polygonization, different mitigation measures have been studied in the last years. A frequently used passive strategy has been to re-profile wheels, [2]. Improving the technology of manufacturing and assembling the wheel rims as a potential remedy is discussed in [22]. Reducing the tangential wheel–rail contact forces by applied friction modifiers may be another universal countermeasure for any vehicle type, [1]. Repairing wheel polygonization with brake shoes or tread cleaners is a more practical approach, [2]. Another approach is to harden wheel treads, [2; 3]. This may result in reduced growth rates of high-order polygonization. Although the associated problems may still be present. Optimizing the rail–wheel profile combination to reduce the evolution of wheel polygonization can be another approach, [10].

A dynamic vibration absorber (DVA), also called a tuned mass damper (TMD), is a well-established system that has been widely used to attenuate undesirable vibrations of mechanical structures at particular excitations ('fixed frequency'), [23; 24]. DVA is a vibration system that works as a passive secondary oscillatory system, applied to a primary system to absorb and dissipate vibration energy. The short review of wheel polygonization in curves with small radius at curvature at trams above has pointed out the significant influence of the second bending mode of the wheelset ('fixed frequency') on wheel polygonization. By applying a dynamic vibration absorber on the wheelset, (1) the onset of self-excited vibrations of the wheelset with respect to the effect of the falling friction effect may be avoided and (2) the wear evolution of predominant orders caused by forced excitation due to initially OOR wheels in the frequency range of the second bending mode may be reduced essentially. As a consequence, effective mitigation of the wheel polygonization at the specific tram line might be achieved. A basic understanding of the mechanism and the performance of a vibration absorber attached to the wheelset as a countermeasure of polygonal wheels is lacking in the scientific literature and will be the focus of this paper. The dynamic properties and the evolution tendencies of predominant polygonal orders of tram wheelsets attached with DVAs during negotiating in curves with a small radius of curvature will be analysed by simulation.

In the next section, a 3-DOF system model is introduced. It will help to improve the understanding of the system behaviour and the mechanism of the dynamic vibration absorber attached at the tram wheelset. Parameter combinations of the dynamic vibration absorber and their influences on the stability in first approximation will be discussed. Bifurcation theory and continuation method will be applied to gain further insight into the effects of key parameters. In particular, the influence of the damping and the stiffness of the vibration absorber on self-excited vibrations and the amplitudes of occurring limit cycles will be revealed. Parameter combinations are identified where self-excitation is suppressed for a realistic range of parameters. Further, a potential reduction of the amplitudes of the resonance phenomena associated with the second bending mode of the wheelset and caused by forced excitation due to initially OOR wheels is discussed. Based on the findings of the basic system model, a well-tuned absorber is attached on the wheelsets of a more detailed system model of a two-axle tram bogie to evaluate the efficiency of the DVA. Dynamic properties of the wheelset and the evolution tendency curves of the outer and inner front wheel with and without a DVA attached at the wheelset are presented. Finally, concluding remarks will be given.

Basic system model

A basic 2-DOF model, representing the leading wheelset of a tram bogie with non-driven, independently rotating resilient wheels, has been introduced in [16]. This system model constitutes a simple, yet fundamental model to study the influence of key parameters on the vibrational behaviour with respect to the lateral dynamic behaviour of the free-rolling wheelset negotiating a sharp curve.

The model considers the leading wheelset of the tram bogie, as shown in Figure 8 more clearly, during steady-state constrained curving, where the outer wheel and the rear inner wheel are in flange contact and may be considered to be constantly aligned with the rail. The bogie frame guides both wheelsets and, therefore, corresponding angles of attack arise. At the leading wheelset the angle of attack is denoted by γ.

The contact mechanics and the coupled oscillations of the leading wheelset are represented by the model of Figure 1. By applying a dynamic vibration absorber to the primary

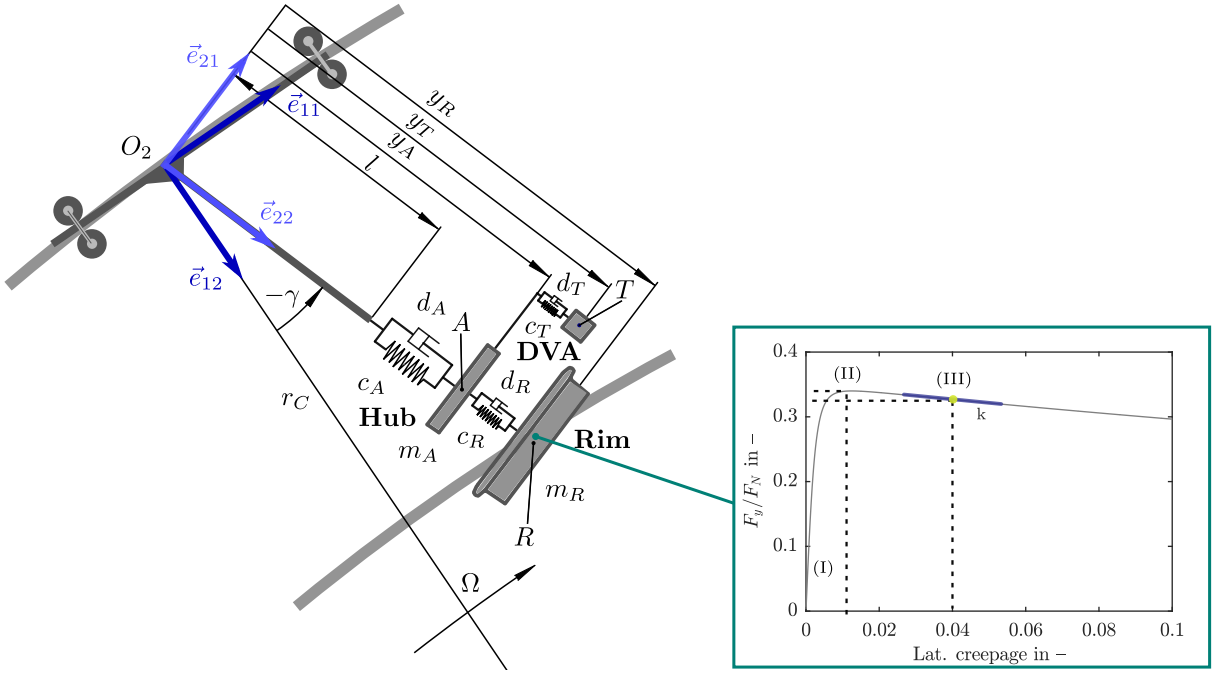

Figure 1. Dynamic vibration absorber attached to minimal model and lateral creep force–creepage characteristics, adapted from [16].

system insights into the effect of its key parameters can be gained. The lateral motion of the primary system is represented in the model by the state variables y_A and y_R assuming that a lateral motion of the contact point of the inner wheel can be excited by the compliance of the wheelset axle and the resilient wheel. The motion of the DVA is represented by the state variable y_T. The considered effective lateral motion y_A comprises contributions from the elasticity of a common axle with two rigid wheels, or as in our case, from bending of the elastic support for the two independently rotating wheels. The considered effective lateral motion of the resilient wheel y_R originates from contributions from camber and lateral displacement.

Figure 1 shows all required parameters. The lumped parameters for the lateral motion of the rim w.r.t. the hub are the effective stiffness c_R and the damping coefficient d_R. The effective stiffness c_A and the damping coefficient d_A for the wheelset axle also consider a contribution from the primary suspension. The reduced mass m_A takes the wheelset axle and the wheel hub into account. The equivalent mass of the resilient wheel is m_R. The absorber mass m_T is elastically connected to the wheel hub by a linear spring c_T and damper d_T.

The outer wheel of the leading wheelset is aligned with the outer rail, represented by a circular path of radius r_C. It moves with constant velocity $\Omega\, r_C$ and yaw rate Ω. The lateral dynamic equations of motion read

$$\begin{aligned} m_A\, a_{A_y} = &-c_A(y_A - l) - d_A\, \dot{y}_A + c_R(y_R - y_A) \\ &+ d_R(\dot{y}_R - \dot{y}_A) + c_T(y_T - y_A) \\ &+ d_T(\dot{y}_T - \dot{y}_A) \end{aligned} \tag{1}$$

$$m_T\, a_{T_y} = -c_T(y_T - y_A) - d_T(\dot{y}_T - \dot{y}_A) \tag{2}$$

$$m_R\, a_{R_y} = -c_R(y_R - y_A) - d_R(\dot{y}_R - \dot{y}_A) - F_y \tag{3}$$

with

$$\begin{aligned} a_{A_y} &= \Omega^2 r_C \cos\gamma - \Omega^2 y_A + \ddot{y}_A\,, \\ a_{T_y} &= \Omega^2 r_C \cos\gamma - \Omega^2 y_T + \ddot{y}_T\,, \\ a_{R_y} &= \Omega^2 r_C \cos\gamma - \Omega^2 y_R + \ddot{y}_R \end{aligned}$$

F_y is the lateral creep force, described with Polach's formulation for the lateral creep force–creepage characteristics, [25]. It acts at the wheel–rail contact of the inner wheel. The lateral creepage ν_y for the inner wheel is given by

$$\nu_y = \frac{\dot{y}_R - V_c}{V_0} \tag{4}$$

with $V_c = \sin\gamma\, V_0 \approx \gamma\, V_0$. V_0 is the rolling speed of the inner wheel. The coefficient of friction μ is determined by

$$\mu = \mu_0 \left[(1 - A)\, \mathrm{e}^{-B\nu_y} + A\right] \tag{5}$$

$A = \mu_\infty/\mu_0$ is the ratio of the friction coefficients with μ_0 as the maximum friction coefficient and μ_∞ defined at infinite slip velocity. Coefficient B is the exponential friction decrease. The resulting lateral creep force–creepage characteristics with nominal parameters in Table 1 are shown in Figure 1.

Stability in first approximation

A small perturbation of the steady-states during curving with constant yaw rate Ω and constant angle of attack γ is presumed. Therefore, the equations of motion, (1), (2), and (3) are linearised with respect to the corresponding steady-states in the falling regime for the considered sharp curve. The steady-states are denoted by index 0. The linearisation of the lateral creep force–creepage characteristics is determined by the gradient k, similarly to [16],

$$k = \left.\frac{\partial F_y}{\partial \nu_y}\right|_{\nu_{y0}=\gamma} \tag{6}$$

Table 1. Baseline parameters of the minimal model.

Symbol	Parameter	Value	Units
r_C	Curve radius at outer wheel	25.75	m
γ	Angle of attack	-0.04	rad
$\Omega\, r_C$	Running speed of the outer wheel	4.15	m/s
F_N	Normal force	35000	N
m_R	Equivalent mass of wheel rim	125	kg
m_A	Reduced mass of wheelset axle and wheel hub	400	kg
c_R	Effective stiffness coefficient of resilient wheel	4.9×10^7	N/m
d_R	Effective damping coefficient of resilient wheel	9500	Ns/m
c_A	Effective stiffness coefficient of wheelset axle/primary suspension	5.2×10^7	N/m
d_A	Effective damping coefficient of wheelset axle/primary suspension	7250	Ns/m
A	Ratio of friction coefficients μ_∞/μ_0	0.36	-
B	Coefficient of exponential friction decrease	0.7	s/m
μ_0	Coefficient of friction	0.35	-

The lateral creep force of the free rolling inner wheel with rolling speed $V_0 = \Omega(r_C \cos\gamma - y_{R0}) \approx \Omega(r_C - y_{R0})$ results to

$$F_y = F_{y0} + k\,(\nu_y - \nu_{y0})\,, \quad \nu_y = \dot{y}_R/V_0 - \gamma \tag{7}$$

The linearised equations of motion for small perturbations $\Delta\underline{y} = \underline{y} - \underline{y}_0$ with state-vector $\underline{y} = [y_A, y_T, y_R, \dot{y}_A, \dot{y}_T, \dot{y}_R]^{\mathrm{T}}$ read in state-space representation

$$\Delta\dot{\underline{y}} = \mathbf{A}\Delta\underline{y} \tag{8}$$

with system matrix $\mathbf{A}$ in the Appendix. In Table 1 the baseline parameters of the minimal model are listed.

The influence of the DVA on the stability behaviour of the minimal model in first approximation is discussed now. For this purpose, the mass of the absorber is selected in advance in order to achieve a compromise between the additional weight of the unsprung mass at the bogie and the amplitudes of the motion of the absorber. Stability maps are derived analytically by applying the Routh-Hurwitz criterion, [26], based on the characteristic equation of (8), which is of 6th order. Setting the Hurwitz determinant $H_5 = 0$ and the coefficient of the characteristic equation $a_6 = 0$, yields the oscillatory marginal and monotone marginal stability, respectively. These expressions are evaluated numerically in Figure 2. In Figure 2(a) the boundaries of stability are presented as a function of the effective stiffness coefficients, c_R and c_A. Static instability (divergence) occurs only for very small parameter values, which are unrealistic from a practical application point of view, and will not be further taken into consideration. The baseline configuration of the model, Table 1, is marked by a black circle. Obviously, the baseline configuration is dynamically unstable with a diverging oscillation (light grey area), when no DVA is attached. The stability boundaries are denoted by ⓪ in Figure 2(a). Note, the effective negative slope of the lateral creep force–creepage characteristics is essential for this behaviour.

A stable behaviour may be achieved at the baseline configuration, by adding a DVA. Figure 2(b) depicts the behaviour of the baseline configuration as a function of different DVA parameter combinations. For specific combinations of the absorber stabilization is achieved (dark grey area). A higher damping coefficient d_T allows a higher stiffness coefficient c_T (black line). Interestingly, the area of stiffness combinations, c_A and c_R, where a dynamically unstable behaviour with diverging oscillations occur, becomes smaller in Figure 2(a), when the stiffness coefficient of the absorber c_T is reduced at constant damping coefficient $d_T = 7500\,\mathrm{Ns/m}$. This behaviour is illustrated for four absorber parameter combinations. Corresponding stability boundaries and their parameter combinations are denoted by ①–④ in Figure 2(a) and in Figure 2(b) respectively. Note, in contrast to parameter combination ②–④, the baseline configuration, black circle, is still dynamically unstable with a diverging oscillation at the parameter combination ①, $c_T = 4 \times 10^7\,\mathrm{N/m}$.

In the next section, a more systematic approach is shown to analyse appropriate parameter combinations of the DVA by investigating the nonlinear system behaviour.

Numerical analysis of the Hopf bifurcation

To gain further insight into the effects of the DVA parameters, the behaviour of the nonlinear model with the nonlinear creep force–creepage characteristics is assessed before and after the loss of stability by means of numerical continuation of the periodic solutions bifurcating from the Hopf bifurcation curves, using the numerical software package MatCont, [27].

Without the DVA, a family of stable periodic solutions (black solid line) with small amplitudes are found between the two supercritical Hopf bifurcation points, around $c_A = 4.8 \times 10^7\,\mathrm{N/m}$ and $c_A = 1.9 \times 10^8\,\mathrm{N/m}$, which coexist with the unstable steady-state solutions (black dashed line), [16], Figure 3. Points H represent the Hopf bifurcation points. For small and (very) large effective wheelset axle stiffnesses c_A, no limit cycles appear; in between, amplitudes do not change significantly, with smaller amplitudes for larger c_A. The motion of the wheel rim y^*_{R0} is normalised with y_{R0}.

The positions of the Hopf bifurcation points shift when the DVA is attached to the wheelset, coloured lines in Figure 3. The range of axle stiffness configurations c_A of unstable steady-state solutions responsible for the (stable) limit cycles decreases as the stiffness of the DVA c_T is reduced while maintaining constant absorber damping

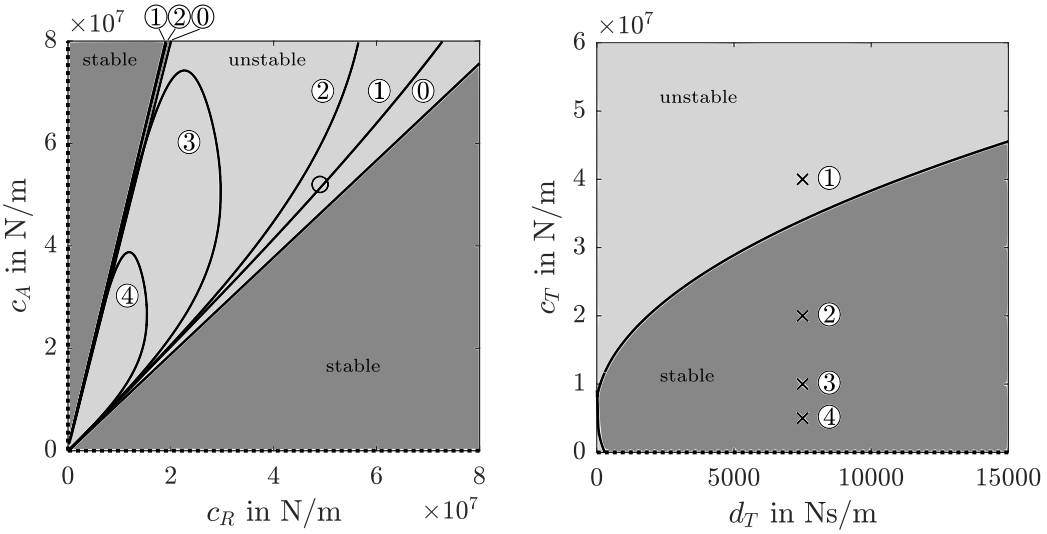

(a) Influence of DVA on the boundaries of stability

(b) Baseline configuration for different DVA configurations

Figure 2. Stability maps.

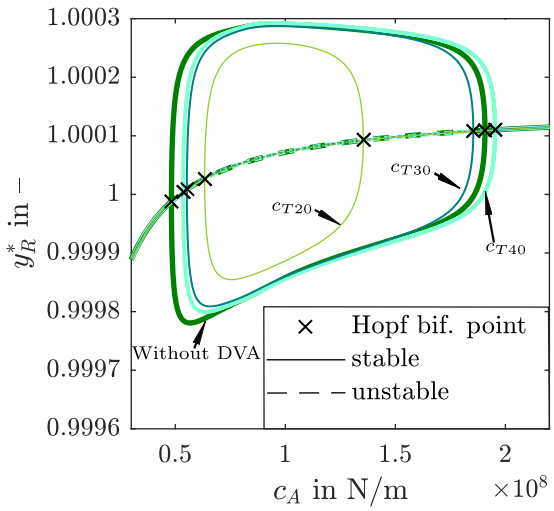

Figure 3. Bifurcation diagram for normalised wheel rim motion y_R^* over effective stiffness c_A of the wheelset axle without and with the DVA for stiffness parameter $c_T = 20 \times 10^6 \mathrm{N/m}$, $c_T = 30 \times 10^6 \mathrm{N/m}$, and $c_T = 40 \times 10^6 \mathrm{N/m}$.

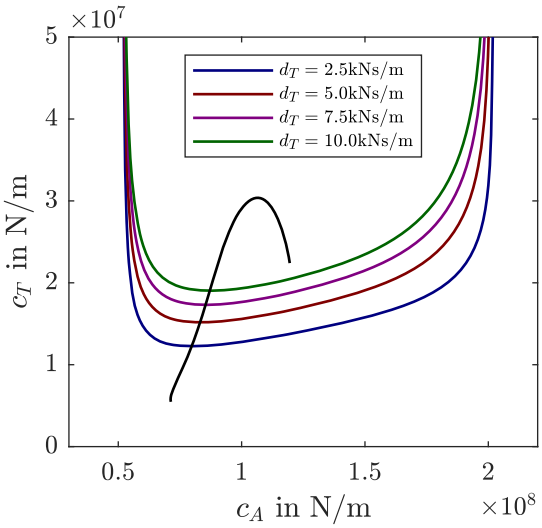

Figure 4. Hopf bifurcation points for stiffness c_T of the DVA over effective stiffness c_A of the wheelset axle; critical Hopf bifurcation points (——).

$d_T = 7500\,\mathrm{Ns/m}$, which confirms the findings above. Additionally, also the amplitudes of stable periodic solutions decrease – only marginally for $c_T = 4 \times 10^7\,\mathrm{N/m}$, brown line, and $c_T = 3 \times 10^7\,\mathrm{N/m}$, blue line, but essentially for $c_T = 2 \times 10^7\,\mathrm{N/m}$, green line.

This behaviour is reviewed in Figure 4. The coloured lines present the Hopf bifurcation points for several DVA damping coefficients d_T. The two Hopf bifurcation points shift towards each other until they merge as the stiffness of the DVA c_T decreases. For $d_T = 7500\,\mathrm{Ns/m}$, the Hopf bifurcation points merge around $c_T = 1.7 \times 10^7\,\mathrm{N/m}$. If the DVA stiffness c_T is reduced even further, the Hopf bifurcation points disappear and no limit cycles occur. The black line in Figure 4 will be discussed later.

Determining the governing equation for the stability limit, i.e. the DVA parameter combinations where the Hopf points merge, allows to define those DVA parameter combinations where self-excitation can be avoided.

Given the above system of ordinary differential equations

$$\dot{\boldsymbol{y}} = \boldsymbol{f}(\boldsymbol{y}, \boldsymbol{\lambda}), \qquad \boldsymbol{y} \in \mathbb{R}^6, \quad \boldsymbol{\lambda} \in \mathbb{R}^2, \tag{9}$$

the parameter values $\lambda_2 := c_T$, for which the Hopf bifurcation vanishes under variation of $\lambda_1 := c_A$, are demanded. A Hopf bifurcation can be detected using the extended system

$$\boldsymbol{f}(\boldsymbol{y}, \boldsymbol{\lambda}) = 0, \tag{10a}$$
$$\mathbf{J}\boldsymbol{u}_R + \omega \boldsymbol{u}_I = 0, \tag{10b}$$
$$\mathbf{J}\boldsymbol{u}_I - \omega \boldsymbol{u}_R = 0, \tag{10c}$$
$$u_{R,k} = 1, \tag{10d}$$
$$u_{I,k} = 0, \tag{10e}$$

The system (10) comprises 20 equations for the unknown variables $\boldsymbol{y}$, $\boldsymbol{u}_R$, $\boldsymbol{u}_I$, ω and λ_1. Equation (10b) and (10c)

are derived from the eigenvalue equation $\mathbf{J}\boldsymbol{u} = i\omega\boldsymbol{u}$, where $\mathbf{J} = \partial \boldsymbol{f}/\partial \boldsymbol{y}$ is the Jacobian matrix, $\boldsymbol{u} = \boldsymbol{u}_R + i\boldsymbol{u}_I$ the eigenvector with its respective real $\boldsymbol{u}_R$ and imaginary $\boldsymbol{u}_I$ parts, and $i\omega$ the critical eigenvalue. There appear two scaling conditions (10d) and (10e) for the eigenvector, because every nontrivial complex multiple of the eigenvector is also an eigenvector. For numerical reasons, index $k \in \{1, \ldots, 6\}$ should be ideally the index of the largest component of the critical eigenvector $\boldsymbol{u} = \boldsymbol{u}_R + i\boldsymbol{u}_I$. By varying a second parameter λ_2 the first parameter λ_1 changes and it may happen, that the Hopf bifurcation vanishes for some special value of λ_2. In this case, a pair of complex eigenvalues $(\sigma, \overline{\sigma})$ would approach the imaginary axis, touch it tangentially and turn back. At the critical point the equation

$$\frac{\partial \operatorname{Re}\sigma}{\partial \lambda_1} = 0 \tag{11}$$

holds. In order to determine the derivative of σ w.r.t. λ_1, the derivative of the equation for the eigenvalue

$$\mathbf{J}\boldsymbol{u} - \sigma\boldsymbol{u} = 0$$

w.r.t. λ_1 is formed. Here it must be taken into account that also $\mathbf{J}$ and $\boldsymbol{u}$ depend on λ_1:

$$\frac{\partial(\mathbf{J} - \sigma\mathbf{E})}{\partial \lambda_1}\boldsymbol{u} + (\mathbf{J} - \sigma\mathbf{E})\frac{\partial \boldsymbol{u}}{\partial \lambda_1} = 0. \tag{12}$$

The second term can be eliminated using the critical left eigenvector $\boldsymbol{\psi}^{\mathrm{T}}$ at the bifurcation point using the dual or adjoint equation

$$\boldsymbol{\psi}^{\mathrm{T}}\mathbf{J} - \sigma\boldsymbol{\psi}^{\mathrm{T}} = 0$$

with proper scaling conditions, e.g. $\psi_k = 1$. Therefore, the system of equations is extended by 12 further equations. Left-multiplying (12) by $\boldsymbol{\psi}^{\mathrm{T}}$ the equation

$$\boldsymbol{\psi}^{\mathrm{T}}\frac{\partial(\mathbf{J} - \sigma\mathbf{E})}{\partial \lambda_1}\boldsymbol{u} = 0 \tag{13}$$

is obtained. For the real part of $\partial\sigma/\partial\lambda_1$ the quantities

$$\begin{aligned}
A &= \operatorname{Re}\boldsymbol{\psi}^{\mathrm{T}}\mathbf{J}'\boldsymbol{u} = \boldsymbol{\psi}_R^{\mathrm{T}}\mathbf{J}'\boldsymbol{u}_R - \boldsymbol{\psi}_I^{\mathrm{T}}\mathbf{J}'\boldsymbol{u}_I,\\
B &= \operatorname{Im}\boldsymbol{\psi}^{\mathrm{T}}\mathbf{J}'\boldsymbol{u} = \boldsymbol{\psi}_R^{\mathrm{T}}\mathbf{J}'\boldsymbol{u}_I + \boldsymbol{\psi}_I^{\mathrm{T}}\mathbf{J}'\boldsymbol{u}_R,\\
\alpha &= \operatorname{Re}\boldsymbol{\psi}^{\mathrm{T}}\boldsymbol{u} = \boldsymbol{\psi}_R^{\mathrm{T}}\boldsymbol{u}_R - \boldsymbol{\psi}_I^{\mathrm{T}}\boldsymbol{u}_I,\\
\beta &= \operatorname{Im}\boldsymbol{\psi}^{\mathrm{T}}\boldsymbol{u} = \boldsymbol{\psi}_R^{\mathrm{T}}\boldsymbol{u}_I + \boldsymbol{\psi}_I^{\mathrm{T}}\boldsymbol{u}_R
\end{aligned}$$

are introduced, with $\mathbf{J}' = \partial\mathbf{J}/\partial\lambda_1$, in our model

$$\frac{\partial \mathbf{J}}{\partial c_A} = \frac{-\boldsymbol{e}_4 \otimes \boldsymbol{e}_1}{m_A}, \tag{14}$$

and the relation

$$\frac{\partial \sigma_R}{\partial \lambda_1} = \frac{\operatorname{Re}(A + iB)(\alpha - i\beta)}{\alpha^2 + \beta^2} = \frac{A\alpha + B\beta}{\alpha^2 + \beta^2} = 0 \tag{15}$$

is obtained. Figure 5, obtained from solving equations (10) and (15), presents the stiffness/damping combinations of the DVA, black line, where the Hopf bifurcation points merge (critical Hopf bifurcation points). For critical Hopf bifurcation points c_T grows for increasing d_T until $d_T \approx 50000\,\mathrm{Ns/m}$, after which c_T decreases gradually. If the DVA is designed with a parameter combination d_T and

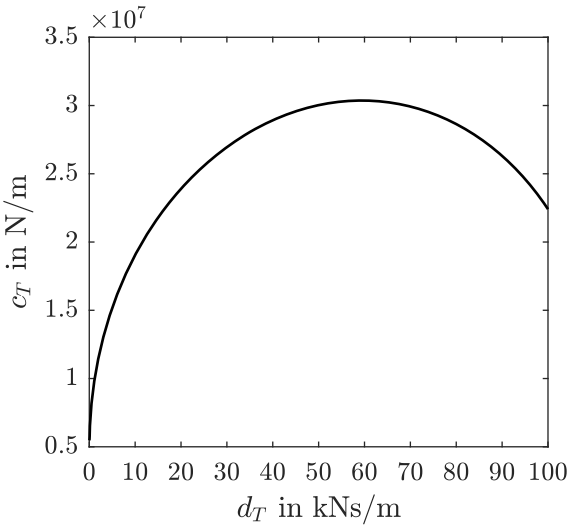

Figure 5. Critical Hopf bifurcation points for stiffness c_T of the DVA over damping coefficient d_T of the DVA.

c_T below this curve no self-excitation is expected. This curve is also indicated by the black line in Figure 4. Figure 6 presents the maximum distance of y_R w.r.t. $L = 1.5\mathrm{m}$, (a), and the maximum acceleration of $\ddot{y}_R$, (b), over the cycle to visualize how the system behaves for varied DVA parameter combinations. The red line represents the critical Hopf bifurcation points, below this curve no self-excitation is expected. For each line, the damping of the DVA, d_T, was held constant, while the stiffness, c_T, was varied. Both diagrams indicate that the respective maxima increase at constant d_T, for increasing c_T. The maxima increase first, close to the hopf point, drastically, then, only marginally, and at the end of the computed parameter range c_T, they do not change significantly.

So far, the parameter range for the DVA, where no onset of self-excitation of the system is expected, has been found. In the next section, the design of the DVA will be studied with respect to forced excitations due to initial wheel OOR. Therefore, the creep force–creepage characteristics is modified in a manner that no self-excitation occurs for the baseline parameter configuration of the wheelset. The coefficient of exponential friction decrease B, from Polach's nonlinear formulation for the creep force–creepage characteristics listed in Table 1, is reduced to $B = 0.4$.

Forced excitation due to initial wheel OOR

A potential mitigation of the wear evolution of predominant orders caused by forced excitation due to initial wheel OOR, as described in the introduction, might be achieved by tuning the DVA to the corresponding dominant structural frequency of the primary system. A well-tuned absorber will resonate out of phase with this structural motion and may reduce resonant vibration amplitudes essentially as its damper dissipates energy, [28]. The efficiency of the countermeasure is illustrated by analysing the frequency response of the basic system model with and without the DVA under forced excitation. The system is assumed to be excited by a harmonic excitation force F_{OOR_y} with frequency ω and constant amplitude η expressed by

$$F_{OOR_y} = \eta \sin(\omega t) \tag{16}$$

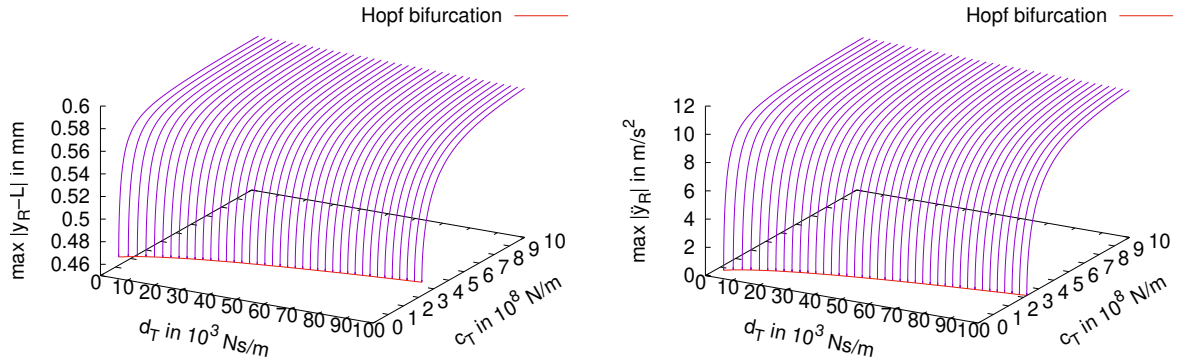

(a) Maximum distance of y_R over one cycle

(b) Maximum acceleration of $\ddot{y}_R$ over one cycle

Figure 6. Stability maps.

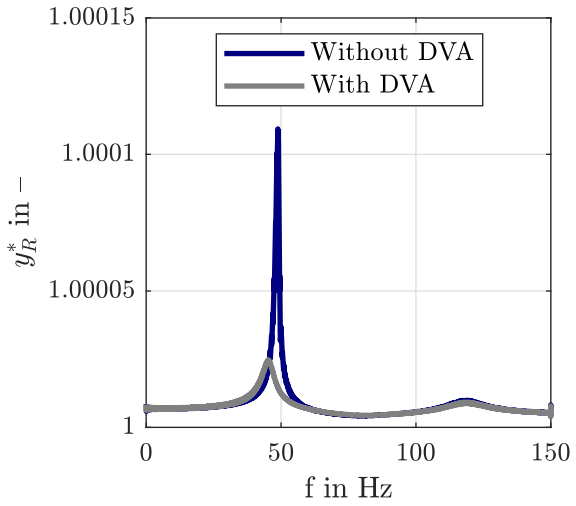

Figure 7. Influence of the DVA on the frequency response.

that originates from the wheel OOR and acts at the wheel–rail contact of the inner wheel in the lateral direction.

The frequency response y_R^*, normalised with steady-state y_{R0}, is computed by sweeping the excitation frequency in the range of interest and is presented in Figure 7. Corresponding to the number of modes of the system two peaks are present, when the DVA is not attached, blue line. The first peak at the blue line is around 50 Hz and corresponds to the flexibility of the wheelset axle. It is significantly greater than the second one around 120 Hz, which can be associated with the resilient wheel.

The design procedure of a DVA for a 1-DOF system was introduced by Den Hartog [29] and was further extended by Thomson [30]. At a multi-DOF system, only one specific mode can be targeted with a dynamic vibration absorber, since it is only effective in a narrow frequency range. If the modes of a multi-DOF system are well separated, the design procedure is essentially equivalent to that of a 1-DOF system, [28]. Here, the resonance amplitude of the mode associated with the flexible mode of the wheelset shall be minimized. For simplicity, Den Hartog's criteria for a 1-DOF system, [29], is utilized to design appropriate parameters of the DVA. They are given in Table 2. Note, with the selected parameter

Table 2. Parameters of the dynamic vibration absorber in the basic system model.

Symbol	Parameter	Value	Units
m_T	Equivalent mass	40	kg
c_T	Stiffness coefficient	4.3×10^6	N/m
d_T	Damping coefficient	6850	Ns/m

combination of the DVA there is no self-excitation expected even if the baseline configuration of the creep force–creepage characteristics, Table 1, is considered, see Figure 5.

Due to the application of the DVA, three peaks corresponding to three modes are expected. Yet, only two distinctive peaks are visible, grey line, in Figure 7. The first distinctive peak is located around 50 Hz and its location (frequency) is slightly shifted in comparison to the configuration without the DVA. Another one is around 120 Hz similar to the blue line. The third peak, which is very close to the frequency of the mode associated with the flexibility of the wheelset around 50 Hz and is not clearly visible. Obviously, the presence of the DVA reduces the amplitude of the resonance peak around 50 Hz significantly. Also, the resonant peak associated with the resilient wheel decreases slightly due to the additional damping in the system.

Generic system model of two-axle tram bogie

In the basic system model above several simplifications and assumptions have been made. Based on the previous findings, the performance of the DVA is now reviewed by discussing dynamic properties w.r.t. self-excitation of the wheelset and the wear evolution of predominant orders w.r.t. forced excitation due to initial wheel OOR in curves with a small radius of curvature with a detailed generic system model of a two-axle tram bogie.

The system model used in this study was presented in [20] and is described here briefly. Only a single, non-driven, low-floor tram bogie is considered for this analysis. Specifically, a car body, a bogie frame located below the centre of the car body, and two wheelsets in axlebridge design with resilient,

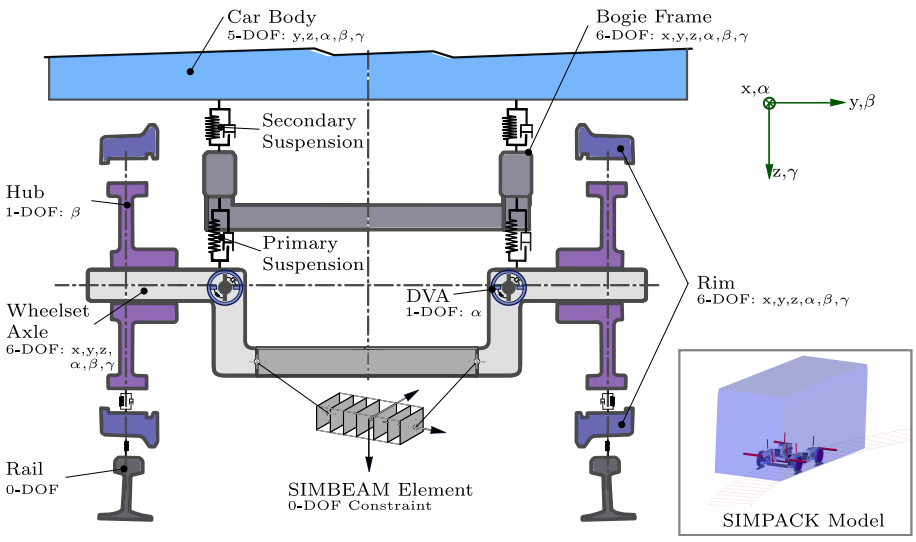

Figure 8. Suspension model of tram with attached DVAs, adapted from [20].

independently rotating wheels are taken into account. The model is set up in the multibody dynamics simulation software SIMPACK, [31], see Figure 8, and comprises rigid bodies, flexible bodies, and interconnection elements (spring and damper elements). Omitted fore and aft cars are substituted by additional support of the car body against the inertial system w.r.t. pitch and roll by torsional spring-damper elements. The car body is attached to a (virtual) 'traction body' that is moved with constant velocity along the track.

The car body and the bogie frame are represented by rigid bodies and connected by bushing elements that represent the secondary springs and dampers. The flexibility of the wheelsets in axlebridge design is accounted for by a linear SIMBEAM element, [31]. The wheel hub and the wheel rim of the wheels are represented by rigid bodies. The elastic layer in between the wheel hub and the wheel rim of the resilient wheel is approximated by linear, massless springs and dampers, that are fixed at coordinate systems of the wheel rim and hub. The Kelvin-Voigt model is utilized. The wheel rim may undergo longitudinal, lateral, vertical, roll, yaw, and torsional motions relative to the wheel hub. Parameters are derived from experimental testing. The primary suspension isolates the wheelsets from the bogie frame and is also modelled utilising bushing elements. Hertzian contact theory [32] is used to derive normal forces, and the FASTSIM algorithm [33] to calculate creep forces in wheel–rail contact problem, respectively. The flexibility of the track is not considered.

In order to damp the second bending mode of the wheelset effectively, both the position and the degree of freedom of the DVA are essential. Either translational or rotational degrees of freedom can be utilized. The position of the absorber should, if possible, be located where the modal amplitude of the critical resonance mode is at its maximum [28]. The analysis of the mode shape of the second bending mode of the wheelset and the minimal model suggests the top of the wheelset in axle bridge design, in close proximity to the bearing of the axle, as an appropriate position of the DVA, see Figure 8. The DVAs are attached on both sides, with a torsional degree of freedom in the direction α; two

Table 3. Main parameters of the torsonal dynamic vibration absorbers in the multibody system model..

Symbol	Parameter	Value	Units
I_T	Moment of inertia	2	kgm^2
c_T	Stiffness coefficient	1.74×10^5	N/rad
d_T	Damping coefficient	300	Ns/rad

DVAs on each wheelset, respectively, four DVAs on the bogie. Their parameters, listed in Table 3, are based on the design parameters of the basic model but are adjusted and optimized (stiffness and damping) by numerical simulation considering the setup of the two torsional DVAs. At the rear wheelset, similar observations have been made w.r.t. self-excited vibrations and evolution tendencies of polygonal wheels in comparison to the front wheelset [10; 16]. Thus, the same parameter design is used at both wheelsets.

Figure 9 shows the influence of the DVA on the vibration amplitudes of the lateral velocity of the inner wheel contact point $\dot{y}_{Rc}$, similar to $\dot{y}_R$ in curves with a small radius of curvature. The vehicle initially runs on a straight track and enters a curve (after 3 s) with a constant radius of curvature of 25 m without passing a transition clothoid. A disturbance occurs after 3 s due to the discontinuity of the curvature. This excites the system and results in vibrations. The longitudinal velocity is set to 4 m/s. The steady-state curving conditions correspond to the previous studies with the basic system model; for the analysis of self-excitation the baseline creep force–creepage characteristics, $B = 0.7$, is assumed again. Without the DVAs, the amplitude of the oscillation increases slowly and a stable limit cycle is reached at about $t = 18$ s. The oscillation frequency is around 55 Hz and the unstable mode can be associated with the second bending mode of the elastic axle of the wheelset. Vibrations also occur for the vehicle with the attached DVAs, but they attenuate very quickly (grey line). This can be attributed to the additional damping introduced by the DVAs. The negative damping with respect to the falling regime in the lateral creep force–creepage characteristics in the system, is no longer sufficient to provoke self-excitation. After a critical, significantly

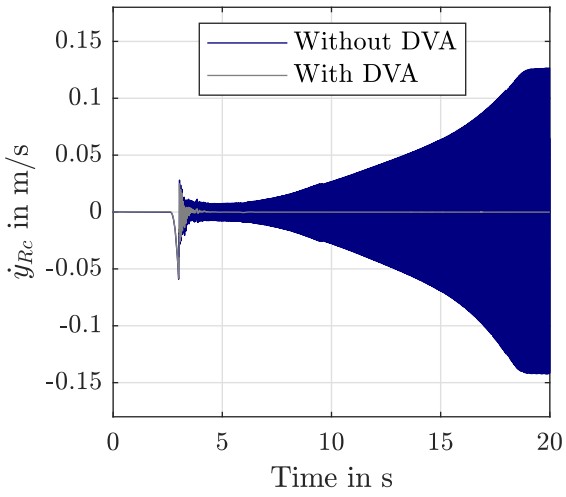

Figure 9. Time history $\dot{y}_{Rc}(t)$ of the lateral motion of the wheel rim contact point with and without attached DVA.

higher, negative slope in the lateral creep force-creepage characteristics is reached, self-excitation may appear once again. Nevertheless, the wheelsets are clearly less prone to self-excitation in curves with small radius of curvature.

The wear evolution of predominant orders w.r.t. forced excitation due to initial wheel OOR may be investigated by a prediction method presented by Peng in [34]. Therefore, the creep force–creepage characteristics is modified as already described above so that no self-excitation occurs for the baseline parameter configuration of the wheelset with B=0.4. Peng's method predicts OOR orders that would grow predominantly at a given speed by means of evolution tendencies curves (ETC) without conducting a closed-loop simulation scheme to account for the changing mutual influence between the OOR wheel and the dynamic wheel–vehicle-track system. It consists of four main steps: (1) input of an initial OOR order, (2) MBS simulation of a dynamic vehicle-track interaction with pre-defined operational conditions where the time history of contact responses is computed, (3) wear model, and (4) output of the evolution tendency. Here, the KTH (Royal Institue of Technology) wear model [35; 36] is applied. The method assumes a linear system behaviour between the initial wheel OOR and the circumferential wheel wear, even though the system dynamics contain non-linear elements. With this in mind, ETCs combine

$$\text{Evolution tendency} = -\cos(\text{Phase}) \times \text{Amplitude} \quad (17)$$

both the Amplitude and Phase spectrum of the wear frequency response function between the excitation, i.e. initial wheel OOR, and the circumferential wheel wear, to provide the evolution direction for specific wheel OOR orders in the considered frequency range. The corresponding phase is the key indicator to determine the amplitude and sign of the evolution tendencies. The wear frequency response function can either be obtained by sweeping the wheel velocity with a fixed OOR order, or, as necessary in curves, by changing the OOR order and performing multiple simulations at constant normal acceleration of the vehicle. If the evolution tendency is above zero, the corresponding initial wheel OOR orders tend to grow, otherwise, they tend to diminish. Evolution tendencies are normalised in the ETC as only the comparison of various frequencies and scenarios are significant. Here, ETCs are normalized w.r.t. the highest absolute value of the evolution tendencies. A higher absolute value of the evolution tendency means faster evolution speed. Consequently, it is expected that distinctive positive peaks in the ETC will lead to orders that will grow predominantly at a given vehicle speed. More information about the method and its simulation scheme can be found in [34] and [10].

Growing and diminishing wheel orders can be identified in good approximation at a given vehicle speed with the relationship

$$\lambda = \frac{2\pi R}{\theta} \qquad v = \lambda f \quad (18)$$

where λ is the wavelength, R is the wheel radius, θ is the polygonal order, v is the longitudinal velocity of the wheel, and f is the excitation frequency.

The influence of the DVAs attached to the wheelsets on the evolution of predominant orders at the outer and inner wheel of the leading wheelset in curves with a small radius of curvature (R=25 m) is presented in Figure 10. The outer wheel is in flange root contact and the inner wheel has a point of contact at the wheel tread. The evolution tendency curves are normalized for the largest absolute value of the evolution tendencies to be one. The evolution tendency curves are dominated by the compliance of the wheelset and fluctuate between two peaks at about 20 Hz (1), 55 Hz (2), and 120 Hz (3) [10]. (1) and (2) can be related with the first and second bending mode of the axle of the wheelset, respectively. The flexibility of the resilient wheel can be associated with (3). Similar observations can be made at the rear wheelset. Increasing the radius of curvature results in decreasing amplitudes at (1) – (3) in the ETCs, but the location (frequency) (1) – (3) does not change. The formation of polygonal wheels in the considered frequency range corresponding to predominant polygonal orders at a given speed is indicated by three distinctive positive peaks associated with the structural modes of the wheelset. In particular, the second positive peak, (2), might lead to predominant orders around 17–20 for typical speeds in curves with a small radius of curvature. If there are significantly lower or even negative evolution tendencies directly before or after the positive peaks, e.g. (2), a more distinct formation of predominated orders is to be expected [34].

The location (frequency) of (1) – (3) shifts slightly compared to the baseline setup (blue line) when the DVAs are attached (grey line). The qualitative shape of the ETCs remains similar but the amplitudes at (2) reduce notably with the attached DVAs. Especially, the second positive peak, (2), at the outer wheel decreases about two thirds essentially by approximately two-thirds. Similarly, there is also a reduction about half, evident at the inner wheel. As a consequence, the development of predominant orders associated with the second bending mode may decelerate significantly. Additionally, the amplitudes at (1) and (3) decrease also slightly.

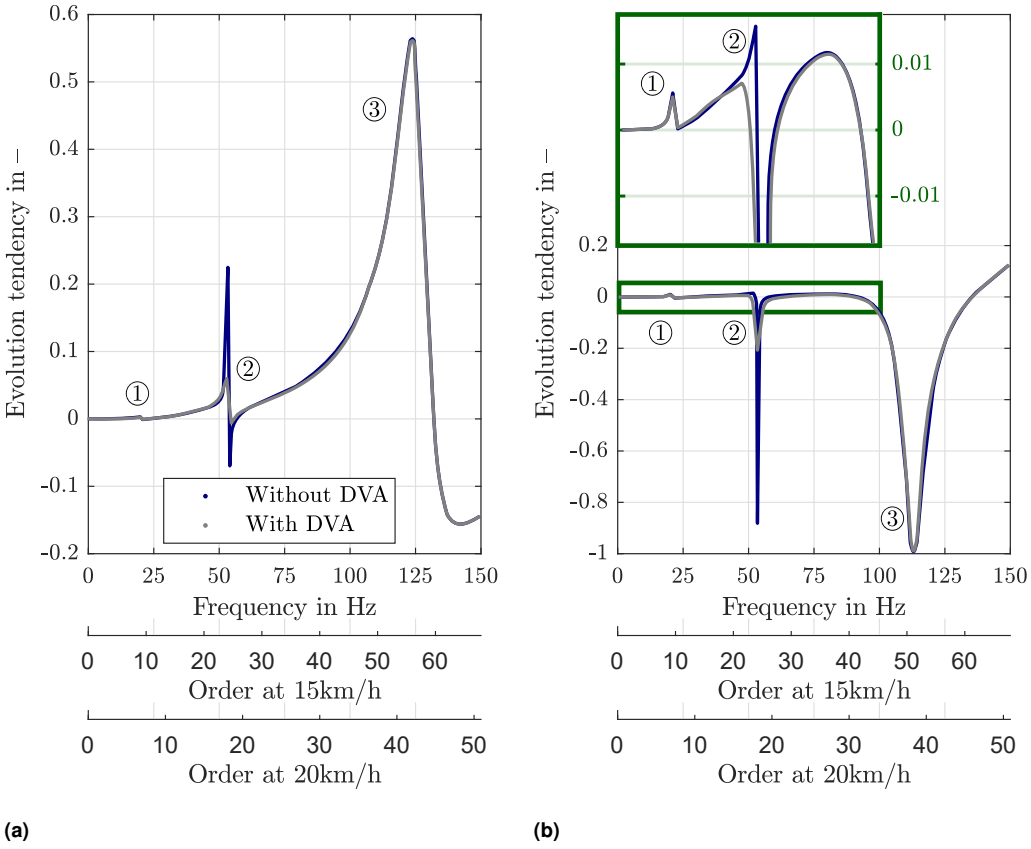

Figure 10. (a) Outer wheel (b) Inner wheel. Influence of the DVAs on the evolution tendency curve with detail (green box).

Conclusions

This paper reports on basic research investigating a possible mitigation mechanism with a dynamic vibration absorber on potential wheel polygonization mechanisms and self-excitation by means of simulation. Both phenomena are associated with the second bending mode of the wheelset at trams in curves with a small radius of curvature. The DVA is considered as a simple countermeasure that does not require significant modifications to wheelsets in place.

A basic 3-DOF minimal model was introduced to analyse the influence of the DVA and its key parameters when it is attached to the wheelset of a tram bogie. Stiffness and damping combinations of the DVA were found where self-excited vibrations of the wheelset w.r.t. the falling friction effect, a potential mechanism for adverse wheel polygonization, are likely to be avoided for a realistic range of parameters. Reducing the stiffness of the dynamic vibration absorber while keeping its damping coefficient constant leads to a system behaviour that is less prone to self-excitation. Further, it was shown that a potential mitigation of the growth of the predominant orders caused by initial wheel OOR may be achieved by tuning the DVA to the structural frequency corresponding to the flexible wheelset axle. A significant reduction of the amplitudes of the resonant vibrations of the wheelset could be shown. A DVA parameter combination was found where self-excitation of the wheelset is avoided as well.

Main findings were reviewed with a more detailed generic system model of a two-axle tram bogie. Based on the findings from the basic system model and a mode shape analysis of the second bending mode of the wheelset axle, an appropriate design of two torsional dynamic vibration absorbers mounted on the top of the respective wheelset was presented. Results from simulations confirmed that the wheelsets are less prone to self-excitations w.r.t. the falling friction effect due to the attached DVAs. Evolution tendency curves, which predict initial wheel OOR orders that will grow predominantly at a given speed, indicated an essential reduction of the evolution speed of wheel OOR orders also associated with the second bending mode of the wheelset.

The detailed design of a DVA device, an integration of the proposed DVA design guidelines into a tram bogie, and accompanied experimental investigations are intended and required to further evaluate the findings from simulations. Wheel polygonization mechanisms related with other wheelset modes, e.g. first bending mode or torsional mode, may be addressed by a similar approach.

APPENDIX

System matrix of 3-DOF model:

$$\mathbf{A} = \begin{pmatrix} 0 & 0 & 0 & 1 & 0 & 0 \\ 0 & 0 & 0 & 0 & 1 & 0 \\ 0 & 0 & 0 & 0 & 0 & 1 \\ -\frac{c_A}{m_A} - \frac{c_T}{m_A} - \frac{c_R}{m_A} + \Omega^2 & \frac{c_T}{m_A} & \frac{c_R}{m_A} & -\frac{d_A}{m_A} - \frac{d_T}{m_A} - \frac{d_R}{m_A} & \frac{d_T}{m_A} & \frac{d_R}{m_A} \\ \frac{c_T}{m_T} & -\frac{c_T}{m_T} + \Omega^2 & 0 & \frac{d_T}{m_T} & -\frac{d_T}{m_T} & 0 \\ \frac{c_R}{m_R} & 0 & -\frac{c_R}{m_R} + \Omega^2 & \frac{d_R}{m_R} & 0 & -\frac{d_R}{m_R} - \frac{k_2 k_3}{m_R V_0} \end{pmatrix}$$

References

[1] Nielsen JC and Johansson A. Out-of-round railway wheels-a literature survey. *Proceedings of the Institution of Mechanical Engineers, Part F: Journal of Rail and Rapid Transit* 2000; 214(2): 79–91.

[2] Tao G, Wen Z, Jin X et al. Polygonisation of railway wheels: a critical review. *Railway engineering science* 2020; 28: 317–345.

[3] Zhai W, Jin X, Wen Z et al. Wear problems of high-speed wheel/rail systems: observations, causes, and countermeasures in china. *Applied Mechanics Reviews* 2020; 72(6): 060801.

[4] Iwnicki S, Nielsen JC and Tao G. Out-of-round railway wheels and polygonisation. *Vehicle System Dynamics* 2023; : 1–44.

[5] Shen W, Song C, Li G et al. Research for high-speed emu wheel hardness and polygon-form relationships with solutions. *Railway Locomotive & Car* 2018; 38(4): 18–23.

[6] Meinke P and Meinke S. Polygonalization of wheel treads caused by static and dynamic imbalances. *Journal of Sound and Vibration* 1999; 227(5): 979–986.

[7] Ye, Shi D, Krause P et al. Wheel flat can cause or exacerbate wheel polygonization. *Vehicle System Dynamics* 2020; 58(10): 1575–1604.

[8] Fröhling R, Spangenberg U and Reitmann E. Root cause analysis of locomotive wheel tread polygonisation. *Wear* 2019; 432: 102911.

[9] Yang X, Li W, Tao G et al. The formation mechanism of high-order polygonal wear of metro train wheels. *Advances in Dynamics of Vehicles on Roads and Tracks IAVSD* 2019; Lecture Notes in Mechanical Engineering. Springer: 704–713.

[10] Zehetbauer F, Edelmann J and Plöchl M. Influences of tram characteristics on wheel polygonal wear evolution. *Engineering Failure Analysis* 2023; : 1–14.

[11] Bethel Lulu G, Chen R, Wang P et al. Random vibration analysis of tram-track interaction on a curve due to the polygonal wheel and track irregularity. *Vehicle System Dynamics* 2020; : 1–23.

[12] Wu X, Rakheja S, Cai W et al. A study of formation of high order wheel polygonalization. *Wear* 2019; 424: 1–14.

[13] Cai W, Chi M, Wu X et al. Experimental and numerical analysis of the polygonal wear of high-speed trains. *Wear* 2019; 440: 203079.

[14] Zhao X, Chen G, Lv J et al. Study on the mechanism for the wheel polygonal wear of high-speed trains in terms of the frictional self-excited vibration theory. *Wear* 2019; 426: 1820–1827.

[15] Wu B, Qiao Q, Chen G et al. Effect of the unstable vibration of the disc brake system of high-speed trains on wheel polygonalization. *Proceedings of the Institution of Mechanical Engineers, Part F: Journal of Rail and Rapid Transit* 2020; 234(1): 80–95.

[16] Zehetbauer F, Edelmann J and Plöchl M. A minimal model to study self-excited vibrations of a tram wheelset in curves with small radius of curvature. *Vehicle System Dynamics* 2023; 0(0): 1–21.

[17] Johansson A and Andersson C. Out-of-round railway wheels—a study of wheel polygonalization through simulation of three-dimensional wheel–rail interaction and wear. *Vehicle System Dynamics* 2005; 43(8): 539–559.

[18] Suarez B, Chover J, Rodriguez P et al. Effectiveness of resilient wheels in reducing noise and vibrations. *Proceedings of the Institution of Mechanical Engineers, Part F: Journal of Rail and Rapid Transit* 2011; 225(6): 545–565.

[19] Lutzenberger S and et al. Formation of wheel polygonisation – analysis of influences from a tramway line. Technical report, Technical Report (not published), 2020.

[20] Zehetbauer F, Edelmann J, Plöchl M et al. Study on potential evolution mechanisms of oor wheels at trams. *Advances in Dynamics of Vehicles on Roads and Tracks II IAVSD* 2021; Lecture Notes in Mechanical Engineering. Springer: 572–581.

[21] Morys B. Enlargement of out-of-round wheel profiles on high speed trains. *Journal of Sound and Vibration* 1999; 227(5): 965–978.

[22] Staśkiewicz T, Firlik B and Kominowski J. Out-of-round tram wheels–multibody simulation study based on measured wheel rim geometry. *Proceedings of the Institution of Mechanical Engineers, Part F: Journal of Rail and Rapid Transit* 2022; 236(1): 122–133.

[23] Sun J, Jolly M, et al. Passive, adaptive and active tuned vibration absorbers—a survey 1995; .

[24] Kela L and Vähäoja P. Recent studies of adaptive tuned vibration absorbers/neutralizers. *Applied Mechanics Reviews* 2009; 62(6).

[25] Polach O. Creep forces in simulations of traction vehicles running on adhesion limit. *Wear* 2005; 258(7-8): 992–1000.

[26] Müller PC and Schiehlen W. *Linear vibrations: a theoretical treatment of multi-degree-of-freedom vibrating systems*, volume 7. Springer Science & Business Media, 2012.

[27] Dhooge A, Govaerts W, Kuznetsov YA et al. New features of the software matcont for bifurcation analysis of dynamical systems. *Mathematical and Computer Modelling of Dynamical Systems* 2008; 14(2): 147–175.

[28] Connor JJ. *Structural motion control*. Pearson Education, Inc, 2003.

[29] Den Hartog JP. *Mechanical vibrations*. Courier Corporation, 1985.

[30] Thompson A. Optimum tuning and damping of a dynamic vibration absorber applied to a force excited and damped primary system. *Journal of Sound and Vibration* 1981; 77(3): 403–415.

[31] SIMPACK. release 2019. https://www.3ds.com/de/produkte-und-services/simulia/produkte/simpack/, Accessed: 2022-05-12.

[32] Hertz H. *Ueber die Berührung fester elastischer Körper*. Walter de Gruyter, Berlin/New York Berlin, New York, 1882.

[33] Kalker J. A fast algorithm for the simplified theory of rolling contact. *Vehicle system dynamics* 1982; 11(1): 1–13.

[34] Peng B, Iwnicki S, Shackleton P et al. General conditions for railway wheel polygonal wear to evolve. *Vehicle System Dynamics* 2021; 59(4): 568–587.

[35] Jendel T and Berg M. Prediction of wheel profile wear: methodology and verification. *Vehicle System Dynamics* 2002; 37(sup1): 502–513.

[36] Enblom R and Berg M. Simulation of railway wheel profile development due to wear—influence of disc braking and contact environment. *Wear* 2005; 258(7-8): 1055–1063.